Effect of specimen size and type on real-mode-I fracture toughness of hooked-end steel fiber-reinforced concrete

Aya S.S. El-Sayed, Ahmed A. Elakhras, Hossam El-Din M. Sallam
Materials Engineering Department, Zagazig University, Zagazig, Egypt
a.saleh23@eng.zu.edu.eg, https://orcid.org/0009-0008-6605-6994
ahmedali.elakhras@gmail.com, https://orcid.org/0000-0002-3821-1327
hem_sallam@zu.edu.eg, https://orcid.org/0000-0001-9217-9957

Ashraf H. Elsafoury
Building and Construction Department, Zagazig Higher Technology Institute, Zagazig. Egypt
ashraf.elsafory@zhiet.edu.eg. https://orcid.org/0000-0001-6615-3083

ABSTRACT. This paper studied the effects of specimen size and type on the real-mode-I fracture toughness (K_{IC})of steel fiber-reinforced concrete (SFRC) specimens. Mode I K_{IC} tests were performed using semicircular bend (SCB) and center-cracked circular disk (CCCD) specimens with different sizes and crack-to-depth ratios, (a/R). SCB Specimens were tested under three-point bending, and CCCD specimens were tested under indirect tension test conditions to achieve pure Mode I crack growth. Moreover, K_{IC} was analyzed as a function of specimen type (SCB and CCCD), specimen size (R values of 50, 75, 100, and 125 mm), and a/R ratios of 0.2, 0.3, 0.4, and 0.5. The results clearly show that the K_{IC} of SFRC exhibits a distinct size effect: it increases with specimen radius up to a critical range of 75-100 mm, after which it levels off. The a/R ratio is an important parameter affecting the toughness; higher values of a/R result in increased K_{IC} values, with increases of 12.9% for CCCD specimens and 22.7% for SCB specimens when a/R is raised from 0.2 to 0.5 at R=75 mm. In addition, the failure mode shifts from ductile fiber pull-out at shallow a/R to brittle fiber rupture at highera/R. The results also emphasize the importance of using geometry-adjusted models, such as Bazant's size effect law (SEL), especially when dealing with SFRC, since fiber distribution and crack-bridging efficiency depend on both size and geometry.

KEYWORDS: Fracture toughness, Size effect, Semicircular bend (SCB), Center-cracked circular disk (CCCD), Matrix crack, Fiber bridging mechanism.

OPEN ACCESS

Citation: El-sayed, S.S.; Elakhras, A.A.; Sallam, H.E.M, Elsafory, A.H., Effect of specimen size and type on real-mode-I fracture toughness of hooked-end steel fiber-reinforced concrete, fracture and Structural integrity, 77 (2026) 27-44.

Received: 25.01.2026
Accepted: 01.04.2026
Online first: 03.04.2026
Issue: 07.2026

INTRODUCTION

Fiber-reinforced concrete (FRC) is a composite material designed to overcome concrete's weakness in tension by using fibers to bridge cracks in the matrix, thereby increasing resistance to fracture. This mechanism is significant because it helps minimize the growth of microcracks within a particulate matrix and macrocracks that affect the entire structure. The material's fracture toughness, primarily Mode I (tensile opening mode), is a major factor affecting its ability to maintain structural integrity; however, it depends on the specimen's geometry and size and exhibits a pronounced size effect. The failure process for FRCs occurs within a defined region, characterized by microcracking and energy dissipation during fracture, known as the Fracture Process Zone (FPZ). This zone significantly influences the measured fracture toughness of the material. Proper precautions must be taken when applying laboratory results to real structures, especially regarding crack growth in FRCs [1,2]. Dolatshahi and Molladavoodi [1] conducted a comprehensive theoretical and experimental investigation into the effect of size on the fracture toughness of cemented quasi-brittle materials. Test results from center-cracked circular disk (CCCD) specimens showed that Mode I, Mode II, and combined Mode I and II fracture toughness values are related to specimen size (i.e., radius). The larger the specimen, the higher the measured fracture toughness. This behavior is consistent with the general behavior of quasi-brittle materials: larger specimens allow more complete development of the FPZ, leading to greater energy dissipation, and, consequently, higher measured fracture toughness values.

A key finding regarding FRC concerns its microstructure. Dolatshahi and Molladavoodi [1] systematically varied the average sand particle size distribution (d50) and linked it to a brittleness index. The d50 is defined as the sand particle size in (mm) at which 50% of the sand particles are smaller, and 50% are larger. As the d50 increases, the likelihood of large sand grains in the cement mortar increases. The higher the d50, the more brittle the material, and the less sensitive the fracture toughness becomes to specimen size. This relates directly to FRC in those fibers, as a secondary distributed-phase-change microstructure and brittleness. More localized failure might be induced by coarser aggregates or a weaker matrix, simulated with an increased d50, reducing the size effect, whereas a strong, fine-grained matrix with good fiber bridging could enlarge the FPZ, thereby increasing the size effect. The d50 concept remains relevant to the microstructure's influence on FPZ development. For FRC, the fiber-matrix interface and aggregate characteristics similarly affect the extent of the FPZ and subsequent size-effect behavior [2]. Guinea et al. [3] developed general equations for fracture toughness (K_{IC}), compliance, and Crack Mouth Opening Displacement (CMOD) in single-edge notched beams under three-point bending. The derived equations can be applied to a wide range of crack-depth and span-to-depth ratios. Even for non-standard geometries commonly used in specialized testing, these equations accurately represent the behavior of FRC specimens [4]. This work provides a solid foundation for future analysis of fracture tests on FRC beams. Mousa et al. [5] performed extensive tests on semicircular bend (SCB) specimens, highlighting their ease of use and applicability to core sample testing. Based on both experimental and numerical investigations, their study identified the span-to-diameter ratio (SDR) of the SCB specimen as the most significant factor affecting both CMOD and the normalized stress-intensity factor. Therefore, the researchers recommended an SDR value of 0.8 when performing three-point bending tests on SCB specimens.

Mousa et al. [5] also found that the ratio of crack length to radius (a/R) determines the shape of the tensile stress zone at the tip of the crack, which closely resembles the FPZ. In terms of FRC, this suggests that fiber bridging efficiency depends on the location and length of the crack with respect to the specimen boundaries. Traditionally, fracture-mechanical testing of FRC has been performed using specimens with a through-thickness crack (TTC). However, this approach is not fully appropriate for FRC because it cuts fibers at the notch surfaces and thus eliminates the crucial fiber-bridging mechanism across the crack[6]. Consequently, the true fracture resistance and energy-absorption capacity of the material are underestimated. In conventional fracture toughness assessments, through-thickness crack (TTC) specimens are frequently employed; however, this methodology inherently disrupts fibers that traverse the crack plane during casting, thereby negating the fiber-bridging mechanism critical to realistic cracking dynamics. Under actual field conditions, fibers persist across both micro- and macro-cracks, thus furnishing crucial post-crack resistance and energy dissipation [6]. To circumvent this constraint, the matrix crack (MC) technique was formulated, allowing fibers to remain continuous across the pre-crack during casting, thereby preserving the inherent fiber-bridging mechanism and facilitating measurement of the real fracture toughness, which accurately represents in-service performance [6].

To address this limitation, Elakhras et al. [6] introduced an innovative MC technique. This approach involves placing a thin foam strip inside the mold during casting to create a pre-crack, while allowing steel fibers to cross the strip, without being severed. Once the foam is removed, the fibers remain intact and retain their bridging capability. This approach

enables the measurement of the true fracture toughness of FRC, fully accounting for fiber contributions both ahead of and behind the crack tip [6].

Fracture toughness measurement in quasi-brittle materials is affected by size and boundary effects. There are two main models to describe these effects; however, there is an ongoing debate between them. Elakhras et al. [6] reported that, although both the MC-FRC and MC-FGC models successfully predicted the size effect in beams, Bazant's size effect law (SEL) proved more reliable when validated using the maximum size nondamaged defect (d_{max}). For SEL predictions, the ratio d_{max}/NMAS (Nominal Maximum Aggregate Size) was close to unity, which is physically consistent, whereas the Boundary Effect Model (BEM) yielded higher and less consistent ratios. The matrix crack method has therefore required the adoption of more robust fracture models. Elakhras et al. [6]successfully used the Equivalent Two-Parameter Fracture Model (ETPFM) on MC-FRC and MC-FGC beams. Their results showed that K_{IC} values obtained from ETPFM matched those derived from the d_{max} concept. The fracture toughness of FRC beams containing 1% steel fibers was over twice that of normal-strength concrete, highlighting the significant contribution of the fiber-bridging when appropriately accounted for. Investigations on the SCB specimens, as recommended by the International Society for Rock Mechanics (ISRM), have demonstrated significant geometric dependences. Different SCB geometries (SCB-1, SCB-2, SCB-3) for pavement materials have also been examined [7]. They found that fracture toughness values varied significantly with geometry, and only the standard SCB-1 specimen yielded reliable K_{IC} values when assessed using the d_{max} concept. This confirms that the measured fracture toughness of pavement material depends strongly on specimen type [7]. Wei et al. [8] showed that the SCB specimen recommended by ISRM proves conservative estimates of K_{IC} for rocks due to the presence of a large FPZ. They indicated that using the initial notch length underestimates fracture toughness and proposed corrections based on an effective crack length that accounts for FPZ development at peak load. Mutnbak et al. [9] demonstrated better performance in lower a/R-ratio specimens, with a larger FPZ and more spread-out fiber action.

Furthermore, it has been found that the K_{IC} calculated using Linear Elastic Fracture Mechanics (LEFM), i.e., based on the equation of mode I stress intensity factor (see Eq. 1), increases with increasing specimen size. For high-strength concrete (98 MPa), K_{IC} increased from 36.61 to 43.71 MPa·mm$^{0.5}$ as the beam depth increased from 80 mm to 240 mm [10]. Ahmad et al. [10] attributed this behavior to changes in compressive strain and the stress gradient with depth, which can hinder crack growth. This size dependency contradicts the fundamental assumption of LEFM, suggesting that factors such as FPZ, which is large with respect to specimen dimensions in smaller specimens, need to be considered. It is worth noting that LEFM assumptions' preliminary focus on the ratio of crack length to specimen depth (i.e., the dimensionless geometric factor) and on the crack length itself. This contradiction arises because quasi-brittle materials such as concrete have a large FPZ relative to the specimen size, during which a significant amount of energy is lost through microcracking and fiber-bridging mechanisms that increase with structure size [1,6]. Therefore, LEFM requires correction factors that account for FPZ development, as illustrated by Bazant's Size Effect Law and the Modified Maximum Tangential Stress (MMTS) criterion [11], to be applicable to such materials. Ahmad et al. [10], on the other hand, proposed a modified stress intensity factor that accounts for beam depth, crack length, and NMAS to correlate experimental data across various specimen sizes and crack depths. Ayatollahi and Akbardoost [11] reported an important study on Iranian white marble that explicitly investigated the simultaneous effects of size and geometry on Mode I fracture toughness using CCCD specimens with different radii. They observed that apparent fracture toughness (K_C) increases with specimen size. To explain this phenomenon, they applied the MMTS criterion, which includes higher-order terms from Williams' series expansion of the crack-tip stress field. Their study emphasized the critical role of the FPZ, defined as a region of microcracking and inelastic deformation located ahead of the crack tip. The relationship between the FPZ size and the specimen's characteristic dimension (e.g., radius or ligament length) influences the size effect. In smaller specimens, the FPZ occupies a greater proportion of the ligament, resulting in nonlinear fracture behavior and reduced apparent K_C values. The MMTS criterion has also been effectively employed to reconcile discrepancies in K_C measured from CCCD and Edge-Cracked Triangular specimens, demonstrating its ability to address geometry effects.

These findings corroborate the observations of Muñoz-Ibáñez et al. [12], who compared the SCB test with a novel Pseudo-Compact Tension (pCT) test on different sandstones and a granite. They found that the effect of specimen size was more pronounced in SCB tests than in pCT. Moreover, K_{IC} results exhibited greater scatter and stronger geometry dependence in smaller specimens, due to material heterogeneity and the relatively larger influence of the FPZ. Standardized testing methods also highlight the importance of addressing geometry effects. AASHTO specifications TP 105-13 [13] utilize the SCB specimens to assess the fracture energy (G_f) and K_{IC} of asphalt mixtures. These standards ensure consistency by imposing strict requirements on specimen dimensions (diameter, thickness, and notch size), loading rates, and conditioning procedures. For complex materials such as FRC, the K_{IC} may vary with geometry rather than remain constant. Therefore, performance-based evaluations incorporating energy dissipation and post-crack behavior may provide a more comprehensive assessment of FRC fracture resistance. This approach is potentially less affected by minor

variations and may better represent field performance. On the other hand, confinement is another important factor that can significantly influence concrete's stress-strain behavior, strength, ductility, and, by extension, its fracture mechanics [14, 15]. This confinement, arising from transverse reinforcement, fiber reinforcement, or external pressure, changes the triaxial stress state in concrete. As a result, the FPZ can become larger, and energy-dissipation mechanisms such as aggregate interlock and fiber bridging can be enhanced. This leads to an increase in both the apparent and actual fracture toughness.

The primary focus of this study is to investigate the fracture toughness of FRC and its relationship with the dimensions and shapes of the test specimens. Although numerous studies have explored various specimen configurations, there remains no consistent method for quantifying the fracture resistance of FRC, particularly when fiber-bridging mechanisms are fully preserved. Recently, some new approaches have emerged using MC instead of TTC for FRC; however, systematic investigations of the combined effects of specimen type (SCB or CCCD), specimen size, and a/R ratio on the actual K_{IC} of steel fiber-reinforced concrete (SFRC) remain limited. Addressing this gap constitutes the main objective of the present work. The novelty of this study is to systematically address this gap by conducting the first known experimental investigation into the combined effects of: specimen type (SCB vs. CCCD), a wide range of specimen sizes (radius R = 50, 75, 100, and 125 mm), and various crack-depth ratios (a/R = 0.2, 0.3, 0.4, and 0.5) on the real K_{IC} of hooked-end steel fiber-reinforced concrete, utilizing the MC technique to ensure the full contribution of fiber bridging is captured.

EXPERIMENTAL WORK

A detailed experimental program was developed to examine how the geometry, dimensions, and initial crack depth of specimens affected the Mode I fracture toughness of steel fiber-reinforced concrete. The following subsections will elaborate on the experimental outline, materials used, the mix design, the casting processes, and the testing configurations for both SCB and CCCD specimens.

Steel Fiber	1% by volume											
Specimens Type	Smooth, S				Central Crack Circular Disk, CCCD				Semicircular Bend, SCB			
Specimens scheme	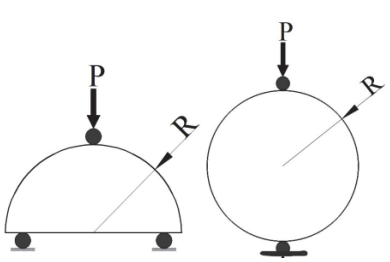				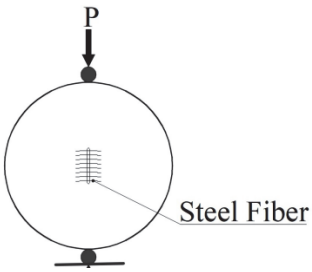				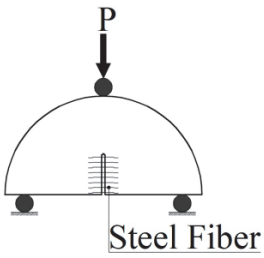			
Radius, R, mm	50	75	100	125	50	75	100	125	50	75	100	125
Thickness, t, mm	25				25				25			
Crack Length, a	0				10	15 22.5 30 37.5	20	25	10	15 22.5 30 37.5	20	25

Table 1: Experimental matrix.

Experimental outline

Tab. 1 outlines the parameters and configurations of the experimental matrix adopted in this work. All specimens contained hooked-end steel fibers at a volume fraction of 1%. The table summarizes the specimen type, includes schematic diagrams of the test setups and geometries, and shows the different specimen dimensions and crack lengths considered in the various testing specimens. Three primary test categories were defined based on specimen geometry and loading configuration. The first one, Smooth (S), refers to CCCD and SCB specimens without pre-existing notches or cracks, which served as controls. The other two categories consisted of prenotched CCCD and SCB configurations. The

CCCD consists of examining circular disk samples with a central notch of length *a* (mm), tested under compressive loading conditions that generated indirect tensile stresses along the crack surface. In contrast, the SCB tests were performed on semicircular samples subjected to three-point bending. The corresponding scheme shows the process, with the supports and the applied load (P).

The size of the specimens, represented by the radius (R)of the circular or semicircular samples, varied across the different experiments. Four distinct radius measurements were considered for S, CCCD, and SCB specimens: 50 mm, 75 mm, 100 mm, and 125 mm. This range enabled systematic evaluation of the size effect across all test configurations. The thickness of each specimen, t, was consistently maintained at 25 mm, regardless of type or radius, to eliminate out-of-plane size effects, in accordance with the assumptions of Bazant's Size Effect Law [16]. Furthermore, the specimen thickness was 25 mm, as specified in AASHTO TP 105-13 [13]. Finally, the crack length defined the initial notch length in CCCD specimens and the edge crack length in SCB specimens. Tab. 1 lists the primary crack lengths considered. It is clear that a/R = 0.2 for all specimen sizes, while for specimen size with R = 75 mm, three additional ratios of a/R have been examined, namely, 0.3, 0.4, and 0.5.

Materials

All concrete mixtures were prepared using ordinary Portland cement (OPC) manufactured by Sina Company. The rating applied was CEM I 52.5 N. Cement testing followed the Egyptian Standard Specification (ESS), (ESS: 2421/2009) [17]. Tab. 2 presents the chemical composition and physical properties of the cement utilized. Siliceous sand and crushed dolomite were used as fine and coarse aggregates, respectively. All aggregates follow the ESS (1109/2002)[18]. The coarse aggregates with a nominal maximum size of 10 mm were washed and left to dry for 24 hours before use, to prevent the effects of fine components. The sand used in this study had a fineness modulus of 2.65. A third-generation high-range water-reducing admixture, MasterGlenium 315C, a modified polycarboxylic ether-based superplasticizer from BASF, was used. Tab. 3 summarizes the physical properties of Glenium as specified in the manufacturer's data sheet (*Certificate No. 0086-CPD-469071 EN 934-2: T3.1 & T3.2*). Tap water free from harmful impurities was used for mixing and curing. Hooked-end steel fibers with a length of 50 mm and a diameter of 1.0 mm were incorporated. The fibers had a tensile strength of 1200 MPa and a density of 7.87 t/m³.

Property	Chemical composition(%)									Physical properties			
Materials	SiO_2	AL_2O_3	Fe_2O_3	CaO	MgO	SO_3	Na_2O	K_2O	L.O. I	S.S m^2/kg	S.W -	I.S min	F.S hrs
OPC52.5 N	21.2	4.67	5.05	64.73	1.5	2.05	0.3	0.22	2.6	350	3.15	80	4

Table 2: Chemical and physical properties of OPC(as provided by the manufacturer): where S.S is the specific surface area, S.W is the specific weight, I.S is the initial setting time, and F.S is the final setting time

Product data	
Appearance	Off-white opaque liquid
Specific gravity at 20°C	1.1 g/cm³
PH-value	6.5 ± 1
Alkali content (%)	≤ 2.00 by mass
Chloride content (%)	≤ 0.10 by mass
Air content	Fulfilled
Water reduction	≥ 112% of Reference mix

Table 3: Physical properties of Glenium used by the manufacturer's data sheet.

Mix design, casting, and curing

The mix proportions are listed in Tab. 4. The quantities of each constituent required to produce 1 m³ of concrete were determined using the absolute volume method, which allowed accurate calculation of fine and coarse aggregate contents. The mixture, as specified in Tab. 4, included 500 kg/m³ of ordinary Portland cement, 200 L/m³ of water, and 1% by volume of hooked-end steel fibers, corresponding to roughly 78.5 kg/m³. The aggregate components were 50% crushed dolomite with NMAS of 10 mm (about 877.3 kg/m³) and 50% siliceous sand (about 877.3 kg/m³. This particular mix was selected to ensure adequate workability and fiber distribution without requiring high A horizontal mixer was used to mix the concrete. In the first step, the dry components (coarse aggregates, fine aggregates, and cement) were placed in the mixer and mixed for about two minutes. After that, steel fibers, water, and superplasticizer were added in a controlled sequence to ensure uniform fiber dispersion. The mixture was then mixed for an additional three minutes to ensure homogeneity. After mixing, the fresh concrete was poured into molds. No external vibration was applied, but compaction

was achieved under self-weight. After that, the filled molds were left at room temperature for 24 hours. After this time, the samples were carefully removed from the molds and placed in clean water for curing for up to 28 days, until ready for testing. Fig. 1 shows the main steps for making and casting the CCCD and SCB samples.

OPC	Water	Steel fibers	Aggregate Type		Aggregates weight	
kg/m^3	Lit/m^3	%	Coarse	Fine	Dolomite, kg/m^3	Sand, kg/m^3
500	200	1	Dolomite	Sand	877.3	877.3

Table 4: Mix design.

Figure 1: The main steps of preparing and casting of CCCD and SCB specimens.

(A) SCB specimens

(B) CCCD specimens

Figure 2: Test setup for (A) SCB and (B) CCCD specimens.

Test setup

All tests were conducted under displacement control at a loading rate of 0.5 mm/min using a testing machine with capacities of 50 kN and 1000 kN located in the Materials Laboratory at the Faculty of Engineering at Zagazig University. The loading, deflection, and CMOD of each test sample were continuously documented with a digital camera. For each configuration (specimen type, R, and a/R ratio), seven identical specimens (replicas) were tested to ensure the repeatability and reliability of the results, and the average values were reported. Fig. 2(A) shows the three-point bending tests of SCB specimens. However, CCCD-type specimens were subjected to axial compression, which induced indirect tensile stress, as shown in Fig. 2(B). The loading of each test sample was continuously documented with a digital camera (Nikon D5300). Image processing was used to measure deflection and CMOD by a digital camera. The timing of crack initiation and growth was recorded for each test sample, enabling a correlation between mechanical response and visual signs of damage. Each loading event was reviewed via frame-by-frame video analysis, enabling very accurate tracking of the crack and the processes leading to failure over long time intervals. To manage the large number of images collected throughout this study, an image selection protocol based on key-event detection methodology, which defined images associated with pre-peak, peak, and post-peak load conditions, was developed to extract the specific frames for detailed analysis. The use of this methodology has enabled a more precise examination of the mechanisms underlying fiber bridging and the evolution of the fracture process zone.

RESULTS AND DISCUSSION

Behavior of smooth specimens

The load–deflection behavior of smooth SFRC specimens tested under SCB configuration is shown in Fig. 3. The figure compares the performance of four SCB specimens with radii (R) of 50 mm, 75 mm, 100 mm, and 125 mm. All specimens contain 1% steel fiber reinforcement. The curves show the entire failure process, from the initial elastic stage to the peak load, followed by the post-peak softening stage. This behavior highlights the crack-bridging contribution of steel. A significant size effect is observed, as the load-bearing capacity increases substantially with specimen radius. The maximum loads recorded for specimens with R of 50, 75, 100, and 125 mm are 7.5, 13, 17, and 20.5 kN, respectively. These results indicate that flexural capacity is strongly influenced by specimen size and geometry, in agreement with structural mechanics principles. All samples exhibit non-brittle, strain-softening behavior after the peak load, typical of fiber-reinforced materials. The load decreases gradually with increasing deflection, reaching maximum deflections of 2.5, 3, 4.2, and 5.5 mm for R = 50, 75, 100, and 125 mm, respectively. This behavior shows that the steel fibers effectively bridge microcracks and, later, a dominant macrocrack, providing the material with residual strength and increasing fracture energy [16,19].

Fig. 4 shows the influence of specimen size on the nominal strength of SFRC, evaluated using two different specimen configurations. The figure shows the ultimate strength (MPa) as a function of radius (mm). The smooth SCB specimens were used to determine flexural strength, whereas CCCD specimens were used to evaluate the indirect (splitting)tensile strength. Both test configurations show that the strength measurements are relatively consistent and decrease as the sample size increases. The SCB flexural strength decreased from approximately 18MPa at R=50 mm to approximately 15MPa at R=125 mm. Similarly, the indirect tensile strength for the CCCD decreased from approximately 9MPa at the small radius to approximately 7.5MPa at the large radius. As the radius exceeded 100mm, the strength values obtained from both configurations tended to converge, indicating that tensile strength measurements for larger samples are less sensitive to the specimen configuration and represent a size-independent property of the material. The negative size effect is a fundamental property of quasi-brittle materials such as concrete and FRC, whose failure is governed by fracture mechanics instead of plastic yield. The observed reduction in nominal strength with increasing specimen size is a fundamental characteristic of quasi-brittle materials, such as SFRC, and is governed by fracture mechanics rather than strength-based criteria. According to Bazant's Size Effect Law [16], this phenomenon occurs because larger specimens can store more strain energy. When a crack forms, this energy is released at a rate that allows the crack to grow at lower nominal stresses compared to the cross-sectional area. As Dolatshahi and Molladavoodi [1] showed, larger specimens allow for a more complete development of the FPZ, where microcracking and energy dissipation occur. Therefore, although the likelihood of encountering larger flaws increases with size, the main factor governing the size effect in SFRC is the energetic scaling of fracture propagation, rather than the statistical distribution of cracks alone.

In smooth SCB specimens containing 1% steel fibers, crack initiation and propagation occur in a stable and progressive manner characteristic of fiber-reinforced composites subjected to a three-point bending test. As the applied load increases, tensile stress develops in the central portion (tensile zone) of the specimen. Initially, no visible cracking is observed.

However, microcracks form within the cementitious matrix, mostly at interfaces between the matrix and aggregates or at pre-existing cracks. The randomly distributed steel fibers initially keep these microcracks from opening. As the load approaches the peak value, microcracks coalesce into a single, larger macrocrack. This crack usually starts in the middle of the tensile face (mid-span), where the bending stresses are maximum. Unlike plain concrete, crack initiation is not sudden or explosive, due to the stress redistribution provided by fiber bridging across the crack faces. After the peak load, the macrocrack spreads up from the tensile face to the loaded curved surface. The crack path is generally tortuous rather than straight, deviating around aggregates and following the weakest region of the matrix. This irregular fracture is due to the arrangement of fibers in the area. The principal process during fiber bridging is that when a steel fiber pulls out of the concrete around the crack, a large amount of energy is required. Thus, fiber bridging does not occur instantaneously. Rather, the process occurs through a gradual decrease in load until the crack reaches ultimate failure. At this point, the fracture surface will appear rough with large amounts of steel fiber debris attached. Besides, a primary large fracture running vertically across the flat surface, typically curved and/or displaced towards one of the support locations as it progresses upward. The primary crack will also typically have a number of additional small cracks located around the main crack, particularly located in the tensile zone, indicating that the fracture propagation occurred over a broad region rather than along a single discrete plane, as shown in Fig. 5.

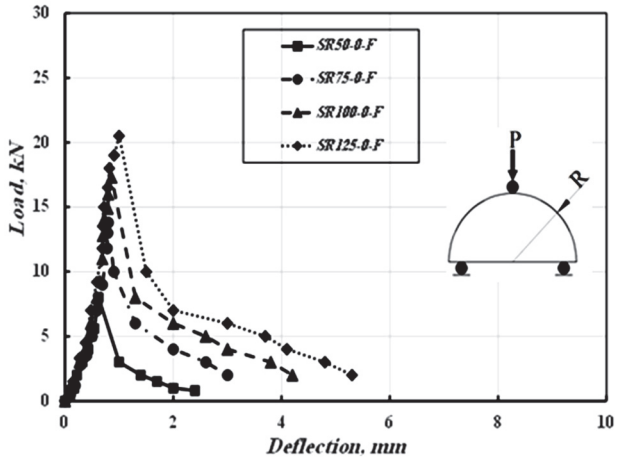

Figure 3: Load-deflection behavior for various sizes of smooth SCB specimens.

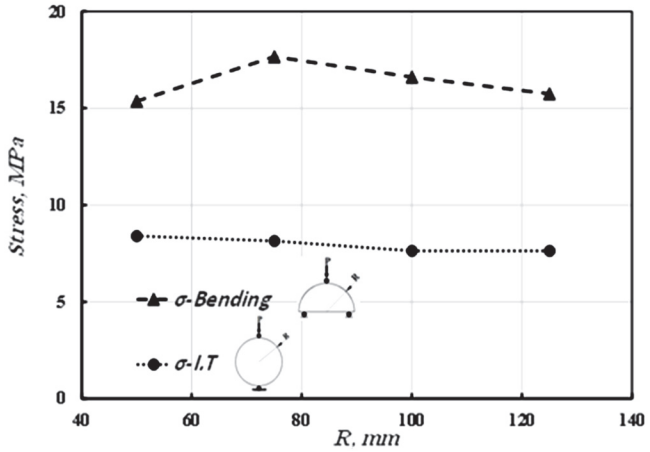

Figure 4: The impact of specimen size on the ultimate strength of SCB and CCCD specimens.

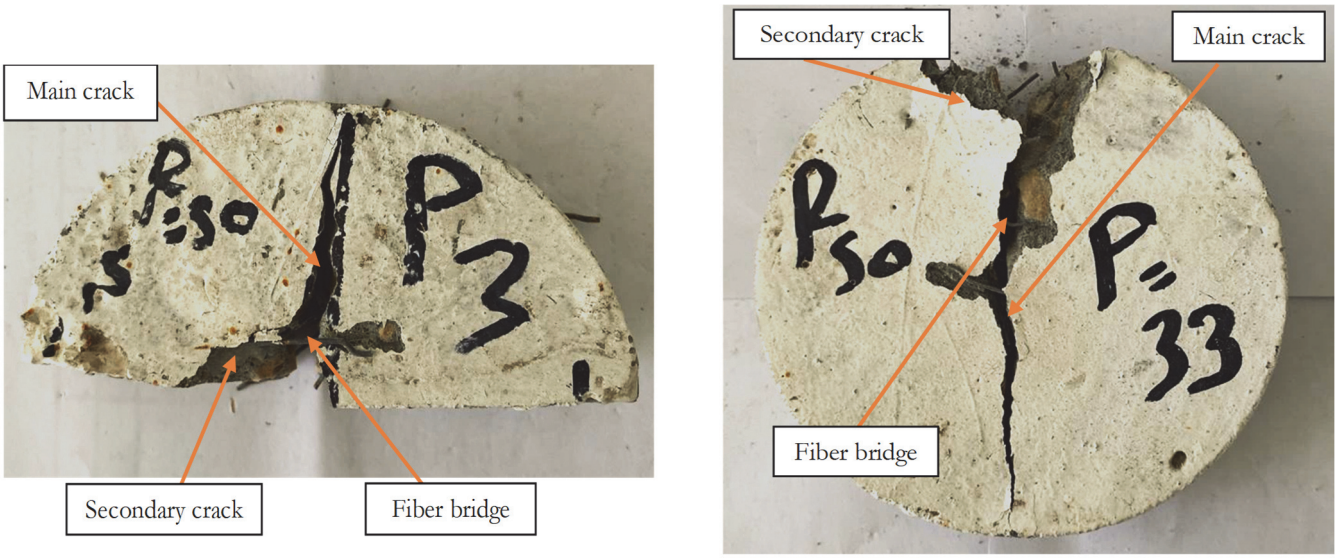

(A) (B)

Figure 5:(A) Failure patterns of smooth SCB specimens; (B) failure patterns of smooth CCCD specimens

CMOD behavior of cracked SCB specimen

In this section, the CMOD behavior of the cracked SCB specimens was examined for different specimen radii at the same a/R, and vice versa, as shown in Figs. 6 and 7, respectively.

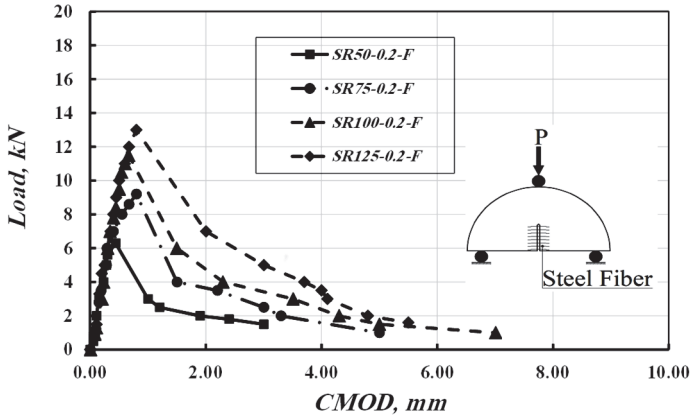

Figure 6: Load-CMOD behavior for various SCB specimen sizes at a/R = 0.2.

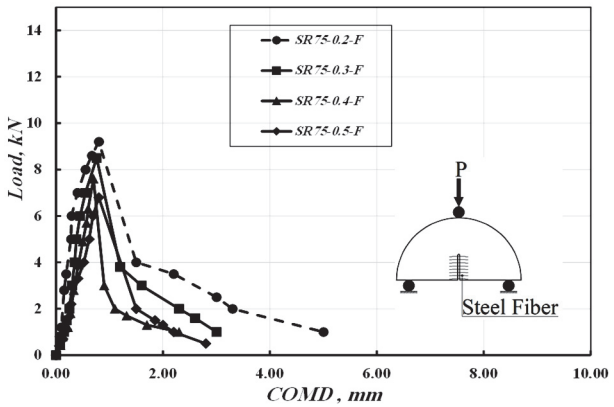

Figure 7: Load-CMOD behavior for various crack-depth ratios of the SCB specimen at R = 75 mm.

Effect of SCB specimen radius on CMOD for the same a/R

Fig. 6 shows the applied load plotted against the CMOD for four different SCB samples: SR50-0.2-F, SR75-0.2-F, SR100-0.2-F, and SR125-0.2-F. All specimens had a constant a/R ratio of 0.2 and contained 1% steel fibers. The curves exhibit an initial linear-elastic rise to the peak load, followed by a strain-softening branch governed by fibers bridging across the crack. This is a typical response for fiber-reinforced concrete under bending conditions. The maximum load increases significantly with the specimen size. The SR50-0.2-F sustains a maximum load of just less than 7 kN, whereas the SR125-0.2-F reaches about 13 kN.

Beyond the peak load, all specimens exhibit a steady decrease in load with increasing CMOD, indicating that steel fibers control multiple cracking. The area under each curve represents the energy absorption capacity, fracture energy. The SR50-0.2-F shows the most brittle drop after the maximum load, although residual load-carrying capacity is still present. In contrast, specimens SR75-0.2-F, SR100-0.2-F, and SR125-0.2-F show a more pronounced and stable post-cracking plateau. These results demonstrate that specimen size influences not only peak load but also the shape and stability of the post-peak softening response. The smaller specimen (SR50-0.2-F) loses load-carrying capacity more rapidly after cracking. The SR100-0.2-F specimen seems to have the best performance after cracking in this set. This suggests that the specimen size, fiber distribution, and crack-bridging efficiency interact in a complex manner. The results show that steel fibers change the material's behavior from brittle to quasi-ductile.

The observed post-peak behavior of SR125-0.2-F, which shows a more significant drop in load despite its larger size, can be explained by statistical variations in fiber distribution and orientation within the larger volume, rather than a violation of the general size-effect trend. Previous studies have shown that the post-cracking behavior of fiber-reinforced concrete is more sensitive to the random distribution of fibers as the concrete specimen size increases [20]. This can lead to localized fiber clustering or alignment, which diminishes bridging efficiency in certain areas. Furthermore, Zhang et al.

[16] demonstrated, through mesoscale modeling, that the development of the fracture process zone in larger SFRC specimens can be adversely affected by nonuniform fiber distribution, leading to early damage localization. The random placement of fibers in larger cross-sections likely explains why the SR125 specimen behaved differently, exhibiting a less consistent increase in post-peak stability than the SR75 and SR100 specimens. Similar trends have been reported in previous studies [21].

Effect of a/R ratio on CMOD for the same SCB specimen radius

Fig. 7 displays the load–CMOD of four specimens with a constant specimen radius (R=75 mm) and varying initial notch depth ratios (a/R = 0.2, 0.3, 0.4, and 0.5). The samples are named SR75-0.2-F, SR75-0.2-F, SR75-0.3-F, SR75-0.4-F and SR75-0.5-F. The curves demonstrate a clear and consistent trend: a deeper initial notch (indicated by a higher a/R ratio) leads to reduced structural stiffness and a significantly lower peak load. SR75-0.2-F exhibits the highest initial stiffness and reaches a maximum load of 9.8 kN. In contrast, SR75-0.5-F exhibits the lowest stiffness and a peak load of 6.7 kN.

After the peak load, all specimens exhibit substantial ductility and residual strength due to steel fiber bridging. The load decreases gradually as the CMOD increases. The post-cracking residual load level is higher for specimens with shallower notches (lower a/R). For instance, at a CMOD of 5 mm, SR75-0.2-F sustains a load nearly three times higher than SR75-0.5-F. The area under the load-CMOD curve up to 2.5 mm for SR75-0.5-F is relatively larger than its peak load, suggesting a more efficient post-peak energy dissipation mechanism, despite the lower absolute load values. Conversely, the shallower-notched specimen, SR75-0.2-F, exhibits higher absolute fracture energy absorption throughout the entire 5 mm deformation range. This is attributed to its greater uncracked ligament, which facilitates enhanced fiber bridging and pull-out mechanisms. This observation is consistent with the findings of Carpinteri et al. [20], who indicated that the post-cracking response in FRC is largely influenced by the ligament length available for mobilizing fiber interactions.

The primary variable controlling the load-CMOD response is the relative notch depth a/R). The significant decrease in peak load and stiffness with increasing notch depth is consistent with elastic bending theory and basic fracture mechanics concepts. The stress concentration at the notch's tip under loading increases with notch depth. However, once crack propagation begins, fiber bridging becomes the dominant mechanism. A larger uncracked ligament enables more efficient mobilization and distribution of more fibers across the fracture plane, as evidenced by the higher residual strength in shallower-notched specimens. In deeper-notched specimens, the fracture process is localized to a more severely pre-damaged section, limiting the full engagement of the fiber network and promoting more brittle behavior [22,23].

Fracture toughness of SCB specimens

Fig. 8 illustrates the relationship between the specimen radius and the critical fracture toughness (K_{IC})for SCB specimens tested under bending. The specimen radius ranges from 50 mm to 125 mm. The plot includes four distinct series based on the a/R ratio: 0.2, 0.3, 0.4, and 0.5. The effect of specimen size is illustrative for the series with a/R = 0.2 and indicated by the dotted line with circular markers. For the a/R = 0.2 series, K_{IC} from 92.2 at R = 50 mm to 103.5 MPa $mm^{0.5}$ at R = 75 mm. This represents an increase of approximately 22.7%, highlighting the substantial influence of relative crack depth on the measured fracture toughness. Beyond R = 75 mm, the fracture toughness decreases at a lower rate at R = 100 and 125 mm, reaching 101.3 MPa $mm^{0.5}$ at R = 125 mm. This plateau indicates that the sample has reached a critical size at which the recorded toughness becomes less sensitive to geometric scaling. The effect of notch depth is shown at a constant radius of R = 75 mm; the fracture toughness increases significantly from 103.5 to about 127 MPa $mm^{0.5}$as the notch depth ratio increases from 0.2 to 0.5. The K_{IC} for an SCB specimen was determined using Eqn. 1 below:

$$K_{IC} = \sigma_{max} Y \sqrt{\pi a} \tag{1}$$

where σ_{max} is the maximum stress (MPa), a is the notch length (mm), and Y is a dimensionless geometric factor, given by AASHTO TP 105-13 [13].

The observed data highlight the bridging mechanisms provided by the 1% steel fiber reinforcement. SFRC acts almost like a brittle material, with a big FPZ, unlike plain concrete. The increase in K_{IC} with a/R demonstrates how the R-curve (resistance curve) works. In SFRC, the energy required for crack growth increases as the crack grows because steel fibers bridge the crack surfaces, redistributing stresses across the crack and slowing unstable growth.

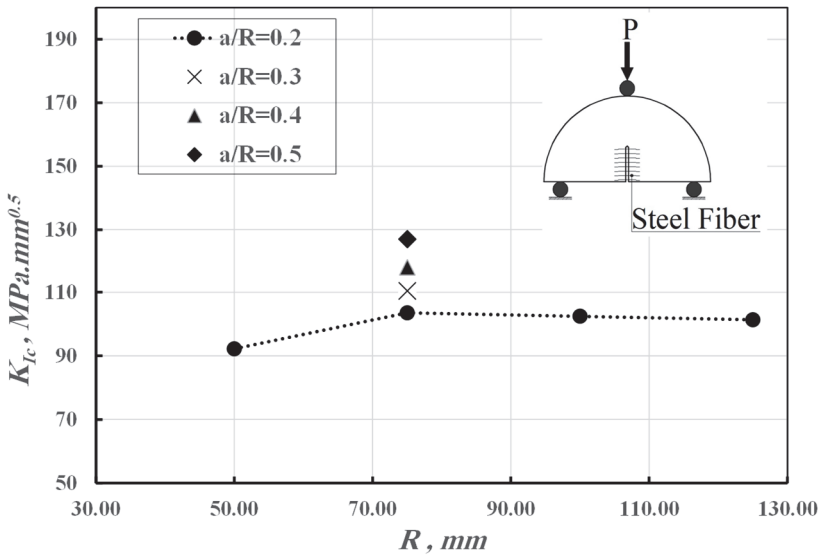

Figure 8: Fracture toughness, K_{IC}, of SCB specimens against the radius R, for different values of a/R.

Mode of failure for SCB specimens

Fig. 9 shows the different failure patterns of prenotched SCB specimens with a/R ratios of 0.2 and 0.5, and all specimens reinforced with 1% steel fibers. The figures show how the size of the initial flaw affects the path of the final fracture. The specimen with a/R = 0.2 (Fig. 9 (A)) exhibits a crack-propagation path that doesn't follow a straight line; instead, it takes a more complex and tortuous path. It can be noted that most of the fibers that cross the crack are slowly pulled out of the material around them, rather than breaking. This behavior indicates effective fiber–matrix bonding and significant energy dissipation through pull-out mechanisms. Fiber pull-out requires much more energy than fiber rupture, resulting in enhanced toughness and ductility.

The observed failure patterns offer distinct visual and quantitative insights into the influence of notch severity on the micromechanics of failure in FRC. With a smaller a/R ratio of 0.2, the bond is larger, resulting in a more widely spread FPZ. In this area, multiple microcracks form, allowing fibers to connect at the crack at varying orientations. This makes it easier for stress to be redistributed, which is beneficial for the ductile, energy-absorbing failure mode consistent with fiber bridging kinetics, reported in previous studies[7,16]. A deeper crack with an a/R of 0.5 (Fig. 9 (B)), on the other hand, severely limits the fracture process to a small, highly stressed area. The failure mechanism is more brittle, consistent with LEFM. The primary crack can't spread evenly because the ligament can't effectively support microcracking. Fibers that cross this rapidly opening crack are subjected to very high stresses and strain rates, increasing the likelihood that they will break rather than pull out [7,16].

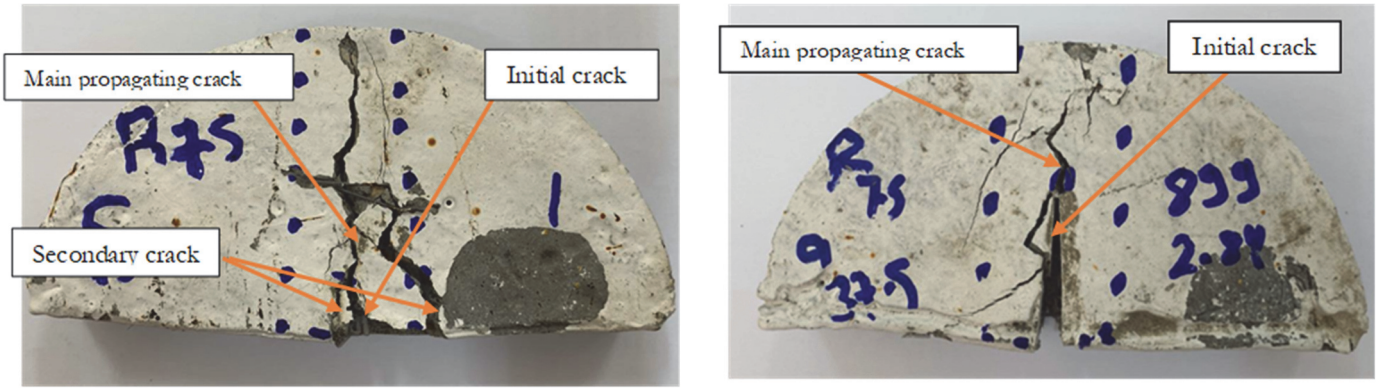

(A) (B)

Figure 9: Failure patterns of cracked SCB specimens for (A) a/R = 0.2 and (B) a/R = 0.5

CMOD Behavior of CCCD Specimens

In this section, the CMOD behavior of the cracked CCCD specimens was examined for different specimen radii at the same a/R, and vice versa, as shown in Figs. 10 and 11, respectively.

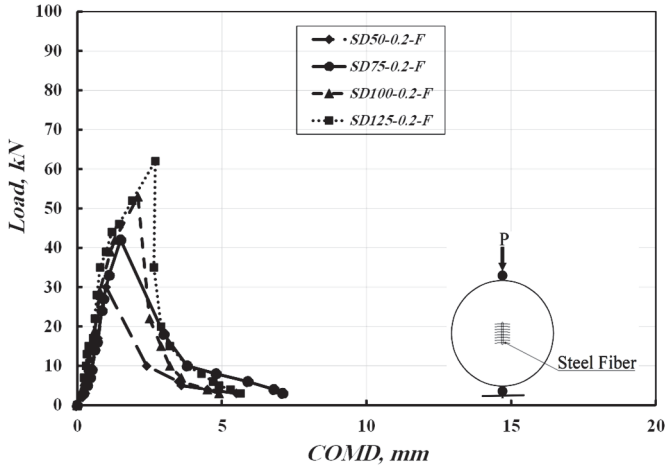

Figure 10: Load-CMOD behavior for different CCCD specimen sizes at a/R= 0.2

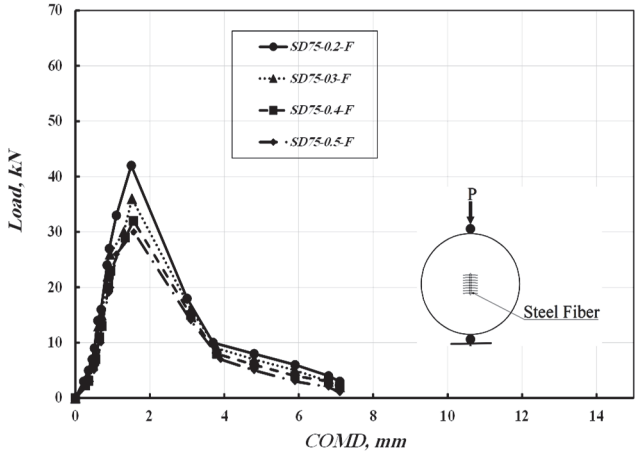

Figure 11: Load-CMOD behavior for different crack-depth ratios of the CCCD specimen at R = 75 mm

Effect of CCCD specimen radius on CMOD for the same a/R

Fig. 10 shows the load-CMOD response of SFRC of four CCCD specimens with different diameters but the same relative notch depths. The samples are named SD50-0.2-F, SD75-0.2-F, SD100-0.2-F, and SD125-0.2-F. All specimens exhibited ductile behavior. This means they had an initial linear-elastic stage up to the peak load, at which the matrix cracked, followed by a strain-softening region in which the applied load was transferred to the fibers, and finally, at larger crack opening, a residual strength plateau is observed.

It is clear that size has a positive effect on the maximum load values. The ultimate load increases with the specimen's diameter. For example, the maximum load for SD50-0.2-F is about 30 kN, while that for SD125-0.2-F is almost 62 kN. After the maximum load, all specimens maintain considerable load-carrying capacity due to fiber bridging, but specimens with a larger diameter consistently exhibit higher residual strength after cracking. Also, the area under each curve is much bigger for bigger specimens. This means that larger SFRC specimens can withstand higher loads and dissipate more energy before breaking, an important trait for structural applications.

These results demonstrate that the size of the specimen has a big effect on FRC failure. However, the fact that post-cracking residual strength and toughness increase with size is especially important for fracture resistance. Two mechanisms contribute to this behavior. First, a larger cross-section provides more room for fiber distribution, increasing the likelihood that fibers effectively bridge the crack and spread stresses along the fracture plane [21]. The FPZ in quasi-brittle materials such as FRC is not merely a static material characteristic; rather, it is a dynamic region of energy dissipation whose extent is directly related to specimen size, thereby influencing fracture mechanics. In smaller specimens, the FPZ can dominate the uncracked ligament, restricting the area where inelastic processes such as microcracking and fiber bridging can develop effectively. This restriction leads to erratic crack growth and a perceived decrease in fracture toughness. Conversely, larger specimens offer the FPZ sufficient room to evolve within a representative material volume, thus enabling the complete activation of fiber-bridging mechanisms at the crack interface. Wei et al. [9] point out that

using the original notch length in LEFM analysis tends to underestimate toughness because it fails to account for the FPZ's role at peak load. They recommend employing an effective crack length that incorporates the fully matured FPZ. As a result, larger specimens tend to exhibit stable, ductile softening behavior and size-independent fracture toughness. This finding aligns with Bazant's Size Effect Law and the plateauing behavior observed in this study, which occurs after a critical radius of about 75–100 mm [23].

Effect of a/R ratio on CMOD for the same CCCD specimen radius

Fig. 11 shows the curves load–CMOD for four cracked CCCD specimens, with a consistent radius of 75 mm but differing in their initial notch depths, as indicated by the a/R of 0.2, 0.3, 0.4, and 0.5. All specimens were reinforced with 1% steel fiber by volume and are designated SD75-0.2-F, SD75-0.3-F, SD75-0.4-F, and SD75-0.5-F. The curves in the figure demonstrate the typical FRC response: an initial elastic loading phase that leads to a peak load followed by a strain-softening stage in which the applied load is supported by fibers bridging across the crack. The results indicated a significant inverse relationship between notch depth and the structural performance. As the notch increases, the ultimate load decreases significantly. The specimen with the smallest notch depth, SD75-0.2-F, reaches the highest peak load, about 60-65 kN, and exhibits the greatest initial stiffness. In contrast, the specimen with the deepest notch, SD75-0.5-F, exhibits the lowest peak load, ranging from 25 to 30 kN, and the smallest stiffness value. This trend supports the idea that the uncracked ligament's depth is the primary geometric factor influencing the load at which the cracked specimen fails.

The marked reduction in stiffness and peak load with increasing a/R ratio effectively demonstrates the fundamentals of LEFM. As the notch depth increases, the stress concentration at the crack tip increases, resulting in a diminished ligament area available to resist the applied load. The behavior observed after cracking highlights the advantages of steel fiber reinforcement. In samples with deeper notches, the fracture process occurs in a region under considerable stress and already weakened, potentially diminishing the pull-out capacity and the overall effectiveness of the fibers. This sensitivity to notch geometry plays a crucial role in material characterization, such as EN 14651, which adopts a fixed a/R ratio (typically 0.2) to ensure consistent and comparable assessments of the fiber contribution, while minimizing the influence of initial defect severity [16].

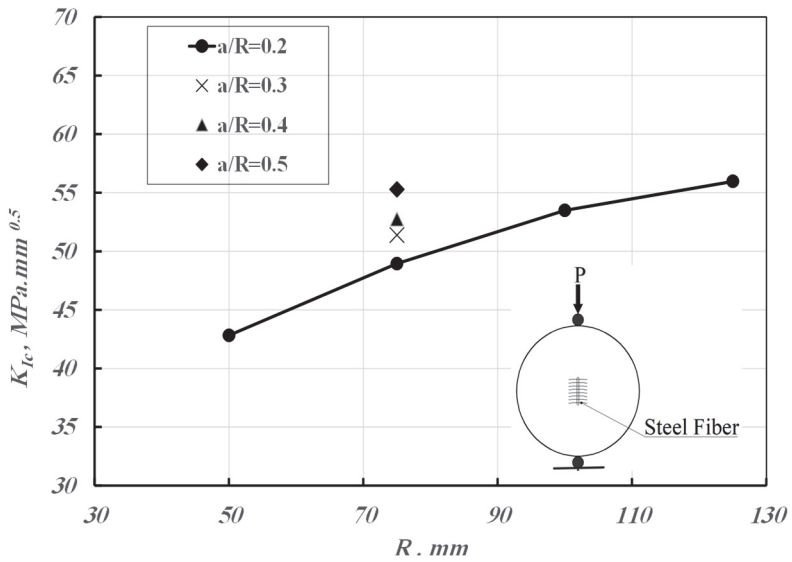

Figure 12: Fracture toughness, K_{IC}, of CCCD specimens against the radius R, for different values of a/R.

Fracture toughness of CCCD specimens

Fig. 12 shows the relationship between the specimen radius and the critical K_{IC} for CCCD specimens subjected to indirect tensile stress conditions. R ranged between 50 and 125 mm. For CCCD specimens, K_{IC} is calculated according to the following Equation[24]:

$$K_{IC} = \frac{P_{max}}{1.772\,Rt} Y\sqrt{a} \qquad (2)$$

where P_{max} is the maximum load (kN), a is the crack length (mm), t is the specimen thickness (mm), and Y is a dimensionless geometric factor.

The figure includes four data series, corresponding to notch depth ratios of a/R of 0.2, 0.3, 0.4, and 0.5. The series for a/R = 0.2 (solid line with circular markers in Fig. 12) demonstrates the size effect. In particular, the K_{IC} increases from 42.8 to 48.9 MPa $mm^{0.5}$ as the R increases from 50 mm to 75 mm. A slower rate of increase is observed between 75 mm and 100 mm, with the K_{IC} value increasing from 48.9 to 53.5 MPa $mm^{0.5}$. At a constant radius of R = 75 mm, increasing a/R from 0.2 to 0.5 yields K_{IC} values of 48.9 and 55.2 MPa·$mm^{0.5}$, respectively, corresponding to a 12.9% increase. The K_{IC} increases further from 55.97 MPa $mm^{0.5}$ to 65.97 MPa $mm^{0.5}$ as the R increases from 100 mm to 125 mm, indicating a gradual reduction in the rate of growth.

The inverse relationship between K_{IC} development and specimen size has been well documented; however, the application in SFRC of the classical Bazant Size Effect Law, which describes the behavior of plain concrete, remains an area of ongoing research. Recent experimental studies, such as those by Fang et al. [25], confirmed a significant size effect in SFRC, although less pronounced than in plain concrete, due to fibers–bridging. The present results support these findings, that even with fiber reinforcement, a distinct size dependence is observable.

Mode of failure for CCCD specimens

Fig. 13 shows the failure patterns of CCCD specimens reinforced with 1% steel fibers with pre-existing a/R values of 0.2 and 0.5. For specimens with a smaller notch depth (a/R = 0.2), the crack path is tortuous and goes around the fibers and aggregates, promoting gradual fiber pull-out and resulting in a more ductile failure mode. In this case, the fracture surface appears rough, indicative of high energy absorption capacity. In contrast, specimens with a deeper notch (a/R = 0.5) exhibit a more straight crack path, leading to a rapid, brittle fracture due to high stress concentrations. In this case, the fibers are more likely to break than to pull out. This makes the fracture surface smoother and reduces the energy dissipation. These results emphasize the critical roles of defect size and fiber-matrix interaction in governing the fracture behavior of SFRC under indirect tensile loading.

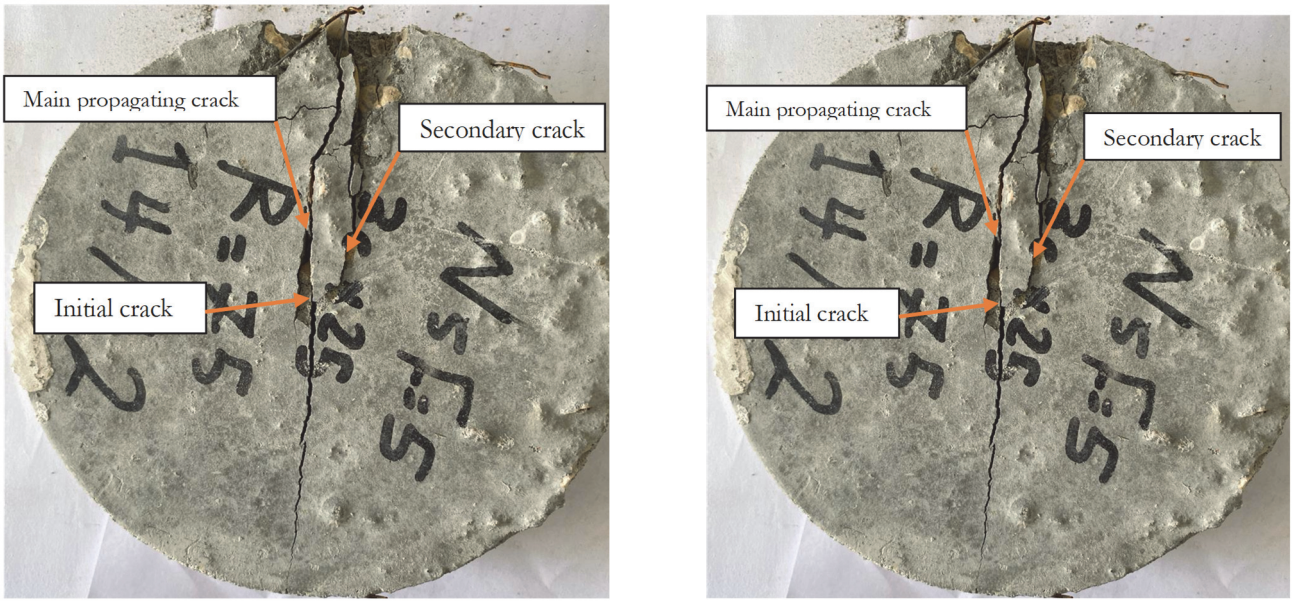

(A) (B)

Figure 13: Failure patterns of CCCD specimens for (A) a/R = 0.2 and (B) a/R = 0.5

Correlation of the effect of specimen type and size by Bazant Size Low (BSL)

Fig. 14 shows the relationship between K_{IC} and for both SCB (SR) and CCCD (SD) specimens. For each specimen type, four a/R ratios are considered: 0.2, 0.3, 0.4, and 0.5. For both specimen types, the BSL trend lines are plotted to illustrate the theoretical size effect on fracture toughness [6]. BSL describes the fracture behavior of quasi-brittle materials, such as FRC and concrete. The energy release linked to a growing FPZ is described as the reason why a notched specimen's nominal tensile strength (f_{in}) decreases as its characteristic size (d) increases. The energy release associated with the FPZ reduces the nominal tensile strength as specimen size increases in quasi-brittle materials such as SFRC. As specimen size

increases, the FPZ becomes relatively smaller than the ligament length, resulting in a more brittle response governed by linear elastic fracture mechanics and thus a lower nominal strength at failure. Here is the governing Equation:

$$f_{tn} = \frac{Bf_t}{\sqrt{1+\frac{d}{d_o}}} \tag{3}$$

where B and do are empirical constants, and f_t is the tensile strength of the matrix. To determine these constants experimentally, Eqn. 3 is rewritten in linear regression form: Y = A X + C, where Y = $(f_{tn}/f_t)^2$ and X = d. So, B = $1/\sqrt{C}$ and do = C/A.After getting B and do, the fracture parameters are calculated. It was found that the effective crack extension of the FPZ (C_f), by using the formula $C_f = do^*g(\alpha)/g'(\alpha)$, where g(α) is the dimensionless energy release function that depends on geometry and relative notch depth, and g'(α) is its first derivative, and α = ao/d. Finally, the K_{IC} was computed by using the following Equation:

$$K_{IC} = Bf_t\sqrt{C_f g'_\alpha} \tag{4}$$

This method allows the prediction of size-dependent fracture properties from tests on geometrically similar specimens of varying sizes.

Data indicate a clear upward trend in fracture toughness with increasing specimen radius for both specimen types; this is typical behavior observed in quasi-brittle size effects. For SCB specimens, K_{IC} increases rapidly for small radii (50-100 mm) and approaches a plateau beyond about 100 mm, indicating a transition toward size-independent fracture resistance. A similar trend was observed for CCCD specimens, but the size effect was generally less pronounced. Across all tested series, higher a/R ratios, such as 0.5, yielded higher fracture toughness due to more effective fiber bridging. The BSL curves fit the experimental data reasonably well, thereby confirming the size-effect law. The results indicate that although fiber reinforcement reduces the size effect relative to unreinforced concrete, a substantial size dependency remains, attributable to the developmental demands of the fracture process zone. The closer correlation between SCB results and Bazant's Size Effect Law suggests that bending-load configurations could provide a more uniform assessment of fiber-bridging mechanisms than indirect tension tests. Consequently, the use of geometry-adjusted models is essential for assessing fracture toughness in fiber-reinforced concrete, as both fiber distribution and crack-bridging efficiency are intrinsically influenced by specimen size and geometry.

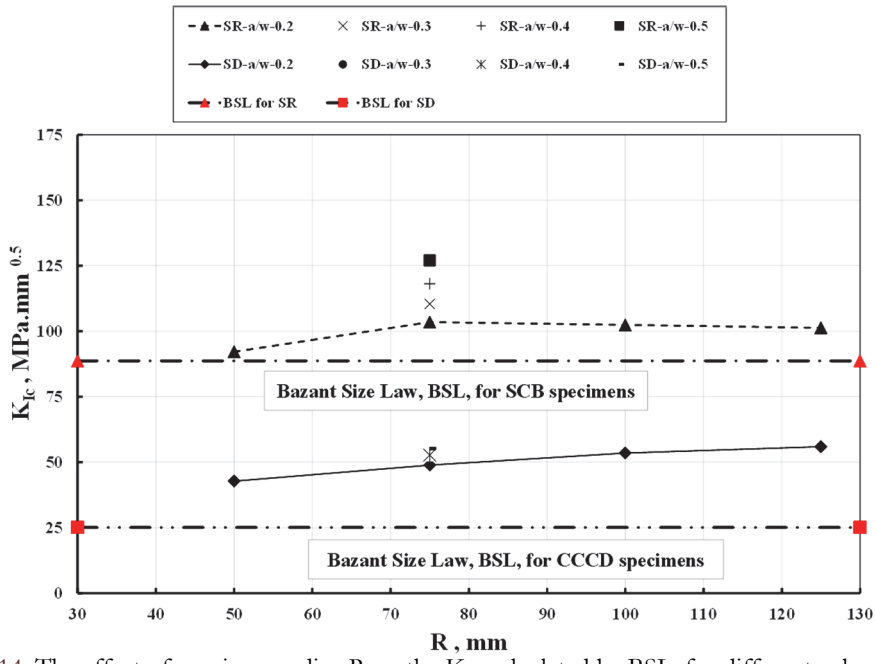

Figure 14: The effect of specimen radius R on the K_{IC} calculated by BSL, for different values of a/R.

CONCLUSIONS

This work presents an experimental investigation of the real-mode-I fracture toughness of fiber-reinforced concrete, focusing on the influence of specimen size and type. Based on the results obtained in the present work, the following conclusions can be drawn:

1. Fracture toughness, $K_{IC,}$ of SFRC exhibits a clear size effect, increasing with specimen radius up to a critical size (75–100 mm), beyond which it approaches a plateau.
2. The notch depth ratio, a/R, significantly influences fracture toughness; increasing a/R from 0.2 to 0.5 leads to an increase in K_{IC} of 12.9% for CCCD specimens and 22.7% for SCB specimens.
3. Fiber bridging in cracked FRC specimens is the primary toughening mechanism, enhancing post-cracking residual strength and energy absorption, especially in larger specimens.
4. The measured K_{IC} values are strongly affected by sample geometry, as CCCD specimens generally exhibit lower K_{IC} under indirect tension loading than SCB specimens.
5. K_{IC} values measured from SCB specimens show a stronger size dependence than those measured from CCCD specimens.
6. To obtain representative fracture properties of FRC that are independent of geometry, standardized tests should explicitly account for specimen size and notch geometry.
7. Future investigations may expand the experimental parameters to encompass a wider variety of fiber types, including macro-synthetic and hybrid fibers, and to include higher volume fractions. Furthermore, advanced numerical modeling, combined with digital image correlation techniques, can enable real-time quantification of fracture process zone development and fiber-bridging mechanisms. Finally, extend this work to evaluate the fracture toughness of self-compacting concrete.

NOMENCLATURE

a	Crack length/notch depth (mm)
a/R	Crack-to-radius ratio
B	Empirical constant in BSL
BEM	Boundary Effect Model
BSL	Bazant Size Law
CCCD	Center-cracked circular disk
CMOD	Crack mouth opening displacement
C_f	Effective crack extension of fracture process zone (mm)
d	Characteristic size/dimension of specimen (mm)
do	Empirical constant in Bazant Size Law (mm)
d_{50}	Mean sand particle size (mm)
d_{max}	Maximum size nondamaged defect (mm)
ETPFM	Equivalent Two-Parameter Fracture Model
ESS	Egyptian Standard Specification
FPZ	Fracture Process Zone
FRC	Fiber-reinforced concrete
f_t	Tensile strength (MPa)
f_{tn}	Nominal tensile strength (MPa)
G_f	Fracture energy
g(α)	Dimensionless energy release function
ISRM	International Society for Rock Mechanics
K_C	Apparent fracture toughness
K_{IC}	Mode I fracture toughness ($MPa \cdot mm^{0.5}$)
LEFM	Linear Elastic Fracture Mechanics
MC	Matrix crack
MMTS	Modified Maximum Tangential Stress criterion
NMAS	Nominal maximum aggregate size

OPC	Ordinary Portland cement
pCT	Pseudo-Compact Tension
P_{max}	Maximum load (kN)
R	Specimen radius (mm)
SCB	Semicircular bend
SDR	Span-to-diameter ratio
SEL	Bazant's size effect law
SFRC	Steel fiber-reinforced concrete
t	Specimen thickness (mm)
TTC	Through-thickness crack
Y	Dimensionless geometric factor
σ_{max}	Maximum stress (MPa)

REFERENCES

[1] Dolatshahi, A. and Molladavoodi, H. (2025). An Experimental and Analytical Investigation of Size Effect on Various Modes of Fracture Toughness of Cemented Quasi-brittle Materials. Rock Mechanics and Rock Engineering. DOI: https://doi.org/10.1007/s00603-025-04919-5.

[2] Mobasher, B., Peled, A. and Pahilajani, J. (2015). Distributed cracking and stiffness degradation in fabric-cement composites. Cement and Concrete Composites, 55, 221–230. DOI: https://doi.org/10.1007/s11527-005-9005-8.

[3] Guinea, G.V., Pastor, J.Y., Planas, J. and Elices, M. (1998). Stress intensity factor, compliance, and CMOD for a general three-point-bend beam. International Journal of Fracture, 89, pp. 103–116. DOI: https://doi.org/10.1023/A:1007498132504

[4] Reza Karimi, H., Bidadi, J., Aliha, M. R. M., Mousavi, A., Mohammadi, M. H. and Haghighatpour, P. J. (2023). An experimental study and theoretical evaluation on the effect of specimen geometry and loading configuration on recorded fracture toughness of brittle construction materials. Journal of Building Engineering, 75, 106759. DOI: https://doi.org/10.1016/j.jobe.2023.106759.

[5] Mousa, S., Mutnbak, M., Saba, A.M., Abd-Elhady, A.A. and Sallam, H.E.M. (2023). Numerical study and experimental validation of the size effect of smooth and mode I cracked semicircular bend specimens. Scientific Reports, 13, 7570. DOI: https://doi.org/10.1038/s41598-023-34201-z.

[6] Elakhras, A. A., Seleem, M. H. and Sallam, H. E. M. (2022b). Fracture toughness of matrix-cracked FRC and FGC beams using equivalent TPFM. Frattura ed Integrità Strutturale, 60, pp. 73-88. DOI: https://doi.org/10.3221/IGF-ESIS.60.06.

[7] Mubaraki, M. and Sallam, H. E. M. (2020). Reliability study on fracture and fatigue behavior of pavement materials using SCB specimen. International Journal of Pavement Engineering, 21(13), pp. 1563-1575. DOI: https://doi.org/10.1080/10298436.2018.1555332.

[8] Wei, M. D., Dai, F., Xu, N. W., Zhao, T. and Xia, K. W. (2016). Experimental and numerical study on the fracture process zone and fracture toughness determination for ISRM-suggested semicircular bend rock specimen. Engineering Fracture Mechanics, 154, pp. 43-56. DOI: https://doi.org/10.1016/j.engfracmech.2016.01.002.

[9] Mutnbak, M., Abbadi, A., Mousa, S., Abd-Elhady, A. A., Sallam, H. E. M. and Reda, R. M. (2025). Effects of specimen geometry and size on mode I and mixed mode fracture behavior of high strength fiber reinforced concrete: Scientific Reports, 15, 15286 DOI: https://doi.org/10.1038/s41598-025-99013-9.

[10] Ahmad, S. S. E., Sallam, H. E. M., EL-Hady, K. M. and Yehia, N. A. B. (1998). Correlation of the effect of beam size and crack-depth ratio in concrete using a modified stress intensity factor, 4th IEC of Faculty of Engineering, Mansura University, C52-C57.

[11] Ayatollahi, M. R. and Akbardoost, J. (2014). Size and geometry effects on rock fracture toughness: Mode I fracture. Rock Mechanics and Rock Engineering, 47, pp. 677–687. DOI: https://doi.org/10.1007/s00603-013-0430-7.

[12] Muñoz-Ibáñez, A., Delgado-Martín, J. and Juncosa-Rivera, R. (2021). Size effect and other effects on mode I fracture toughness using two testing methods. International Journal of Rock Mechanics and Mining Sciences, 143, 104785, DOI: https://doi.org/10.1016/j.ijrmms.2021.104785.

[13] American Association of State Highway and Transportation Officials (AASHTO). (2015). Standard Method of Test for Determining the Fracture Energy of Asphalt Mixtures Using the Semicircular Bend Geometry (SCB) (TP 105-13).

[14] D'Amato, M., Braga, F., Gigliotti, R., Kunnath, S. and Laterza, M. (2012). A numerical general-purpose confinement model for nonlinear analysis of R/C members. Computers & structures, 102, pp. 64-75. DOI: https://doi.org/10.1016/j.compstruc.2012.03.007.
[15] Laterza, M., D'Amato, M., Braga, F. and Gigliotti, R. (2017). Extension to rectangular section of an analytical model for concrete confined by steel stirrups and/or FRP jackets. Composite Structures, 176, pp. 910-922. DOI: https://doi.org/10.1016/j.compstruct.2017.06.025
[16] Zhang, J., Liu, X., Wu, Z., Yu, H., Fang, Q. (2022). Fracture properties of steel fiber reinforced concrete: Size effect study via mesoscale modelling approach, Eng. Fract. Mech., 260, p. 108193. DOI: https://doi.org/10.1016/j.engfracmech.2021.108193.
[17] Egyptian Standard Specification (ESS: 2421/2009). Cement - Physical and chemical tests. Egyptian Organization for Standardization and Quality. *Cairo, Egypt.*
[18] https://www.eos.org.eg/en/standard/15149
[19] Egyptian Standard Specification (1109/2002). Aggregates for concrete. Egyptian Organization for Standardization and Quality. *Cairo, Egypt.* https://www.eos.org.eg/en/standard/288.
[20] Gao, D., Wang, L., Ma, W. (2025). Flexural tensile property and damage evolution of hooked-end steel fiber reinforced concrete with low fiber dosage and concrete strength, Journal of Building Engineering, 99, p. 111680. DOI: https://doi.org/10.1016/j.jobe.2024.111680.
[21] Carpinteri, A., Accornero, F., Rubino, A. (2023). Scale effects in the post-cracking behaviour of fibre-reinforced concrete beams, Int. J. Fract., 240(1), pp. 1–16. DOI: https://doi.org/10.1007/s10704-022-00671-x.
[22] Bhosale, A.B., Prakash, S.S. (2020). Crack Propagation Analysis of Synthetic vs. Steel vs. Hybrid Fibre-Reinforced Concrete Beams Using Digital Image Correlation Technique, Int. J. Concr. Struct. Mater., 14(1), p. 57. DOI: https://doi.org/10.1186/s40069-020-00427-8.
[23] Yoo, D.-Y., Yoon, Y.-S., Banthia, N. (2015). Predicting the post-cracking behavior of normal- and high-strength steel-fiber-reinforced concrete beams, Constr. Build. Mater., 93, pp. 477–485. DOI: https://doi.org/10.1016/j.conbuildmat.2015.06.006.
[24] Hossam El-Din, M.-A., Moawad, M., Ahmad, S., Reda, R.M. (2025). A novel procedure for accurately measuring the Mode II fracture toughness of steel fiber reinforced self-compacting concrete, Fracture and Structural Integrity, 20(75), pp. 200–212. DOI: https://doi.org/10.3221/IGF-ESIS.75.14.
[25] Atkinson, C., Smelser, R. E. and Sanchez, J. (1982). Combined mode fracture via the cracked Brazilian disk test. International Journal of Fracture, 18(4), pp. 279-291. DOI: https://doi.org/10.1007/BF00015688
[26] Fang, G., Wang, Q., Zhang, M. (2021). Micromechanical analysis of interfacial transition zone in alkali-activated fly ash-slag concrete, Cem. Concr. Compos., 119, p. 103990. DOI: https://doi.org/10.1016/j.cemconcomp.2021.103990.